

Optics Letters

Lidar system based on lens assisted integrated beam steering

XIANYI CAO, GAOFENG QIU, KAN WU,* CHAO LI, AND JIANPING CHEN

State Key Laboratory of Advanced Optical Communication Systems and Networks, Department of Electronic Engineering, Shanghai Jiao Tong University, Shanghai 200240, China

*Corresponding author: kanwu@sjtu.edu.cn

Received 1 July 2020; revised 12 September 2020; accepted 19 September 2020; posted 23 September 2020 (Doc. ID 401486); published 13 October 2020

We present a demonstration of solid-state light detection and ranging (Lidar) at 1550 nm by applying integrated two-dimensional (2D) lens assisted beam-steering (LABS) technology. LABS has $O(\log N)$ power consumption for N antennas and allows a simple control complexity with digital signal input. A time-of-flight coaxial Lidar is demonstrated with this beam-steering technology. The integrated beam-steering chip and lens both transmit and receive the light. The Lidar has 16 scanning angles, 19.5 m ranging distance, and a 3 cm ranging error. This Letter proves the potential application of 2D LABS in Lidar and paves the way for a fully integrated Lidar system. © 2020 Optical Society of America

<https://doi.org/10.1364/OL.401486>

Recently, light detection and ranging (Lidar) technology has attracted widespread attention in the fields of sensing [1], robotics [2], autonomous driving [3], etc. Optical beam-steering devices are essential components in Lidar systems to scan a beam to different directions. Many beam-steering technologies have been demonstrated, such as mechanical galvanometers [4], microelectromechanical systems [5,6], liquid crystals [7], and optical phased arrays (OPAs). For solid-state beam steering, the OPA has become a research hotspot. By carefully modulating the light phase in each antenna, the emitted light can interfere constructively in the far field in a specified direction [8]. Much progress of Lidar based on integrated OPA devices has been made for the low divergence angle [9], wide field of view [10–12], and high side-mode suppression [13]. Meanwhile, a new beam-steering technology based on an on-chip switch/antenna structure and an off-chip [14–17] or on-chip lens [18–20] has also received wide attention, known as lens assisted beam steering (LABS). For LABS technology, the incident light is guided to one emitter/antenna by an integrated switch or switch array and emitted to the free space. The beam is then collimated, and its direction is steered after passing through a fixed lens. Beam steering is achieved by switching the beam to different emitters. If a binary-tree switch array is employed, LABS only requires $\log N$ switches to operate simultaneously for N emitters (i.e., power consumption is $O(\log N)$) whereas

the OPA requires all N phase shifters to operate (power consumption is $O(N)$), which significantly reduces the control complexity. A few works of LABS have been reported; however, a Lidar system based on this technology has not been demonstrated yet.

In this Letter, we present, to the best of our knowledge, the first demonstration of a solid-state Lidar based on LABS. The Lidar is designed to operate under a coaxial time-of-flight (ToF) mode at 1550 nm. The coaxial design allows the transmitting and receiving light to share the same light path, and the ToF mode enables a direct detection of the returning signal. The Lidar has 16 scanning angles, 19.5 m ranging distance, and a 3 cm ranging error. This Letter proves the high potential of two-dimensional (2D) LABS in Lidar applications and paves the way for a fully integrated Lidar system.

The principle of LABS is shown in Fig. 1. The emitter (antenna) array coincides with the front focal plane of the lens. Each time only one emitter emits a beam. The beam is collimated by the lens, and the beam direction is also steered. The beams emitted from different emitters are parallel to each other before intersecting the lens. All the beams virtually intersect at a point (denoted as “S”) in the back focal plane of the lens. If the point “S” is considered as a virtual light source, it is obvious that the beam steering can be performed by selecting different emitters to the emit beam. In other words, the location of the emitter in the focal plane of the lens determines the angle to which the beam collimated by the lens is directed. Therefore, the maximum beam-steering angle θ can be expressed as follows [15]:

$$\theta = 2 \tan^{-1} \left(\frac{l}{2f} \right), \quad (1)$$

where l is the length of the emitter array, and f is the focal length of the lens. The beam divergence angle $\Delta\theta$ is given by [15]

$$\Delta\theta = \tan^{-1} \left(\frac{w}{f} \right), \quad (2)$$

where w is the beam size from the emitter. Additionally, the beam-steering step θ' can be approximately expressed as [14]

$$\theta' = \tan^{-1} \left(\frac{p}{f} \right), \quad (3)$$

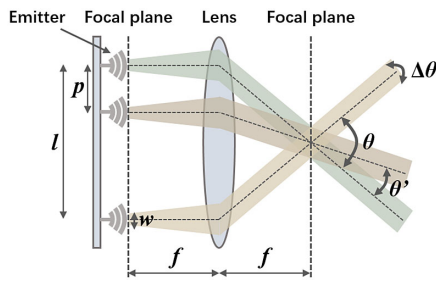


Fig. 1. Principle of LABS.

where p is the distance between two adjacent emitters. The above three equations indicate that different beam divergence, beam-steering angles, as well as beam-steering steps, can be achieved by properly designing the emitter array and lens parameters. A maximum steering angle of 90° can be obtained if a large size of emitter array is employed for a given focal length.

Compared with the OPA which steers the beam continuously, the LABS approach steers the beam discretely, and the gap between each emitter causes the blind zone in the far field. Our previous work has shown that the defocusing method is able to eliminate this blind zone [13].

If we assume that the emitted light is a plane wave and reflected from an isotropically scattering target, the received power is given by [21]

$$P_r \propto \frac{A_r P_t}{R^2}, \quad (4)$$

where A_r is the receiver (RX) area, P_t is the transmitting peak power, and R is the target distance. A large RX aperture is required to overcome the R^2 dependence of the received power.

The structure of the LABS device is illustrated in Fig. 2(a). This LABS device consists of an integrated SiO_2 1×16 switch chip, a 4×4 fiber array, and a lens. The SiO_2 1×16 switch chip is fabricated by a standard planar lightwave circuit technology and has a material stack of $400 \mu\text{m}$ silicon substrate, $15 \mu\text{m}$ pure silica (as bottom cladding), $6 \mu\text{m}$ doped silica (as the waveguide), and $15 \mu\text{m}$ pure silica (as upper cladding). The waveguide has a 0.75% refractive index difference to cladding, $6 \mu\text{m} \times 6 \mu\text{m}$ cross section, and $<0.05 \text{ dB/cm}$ loss. The 1×16 switch has a binary-tree structure consisting of four stages of 1×2 Mach-Zehnder interferometer (MZI) switches. Each 1×2 MZI switch has a $2000 \mu\text{m}$ long / 80Ω titanium thermal heater on one arm as the phase tuner. The switching is achieved by applying a voltage to the heater and changing the waveguide index based on the thermo-optic effect.

A photo of the SiO_2 chip is shown in Fig. 2(b). The measured extinction ratio of a single MZI switch is more than 20 dB, and the measured phase shift versus different electrical voltage is shown in Fig. 2(c). The phase shifter is operated from π to 2π region to avoid the residual phase shift at 0 V voltage. The average V_π is $\sim 4 \text{ V}$. The rise time of the switches in the chip is 1.18 ms, and the fall time is 0.97 ms, as shown in Fig. 2(d). The speed can be improved to microsecond level by using a silicon nitride platform. The chip has packaged single-mode fiber input and outputs. The total insertion loss of this photonic chip is measured to be $\sim 3 \text{ dB}$, including 1 dB fiber coupling loss and 2 dB loss from four cascaded 1×2 switches and waveguides.

All 16 outputs of the chip are connected to a 4×4 fiber array in order to convert the 1D array to a 2D array. This 2D fiber

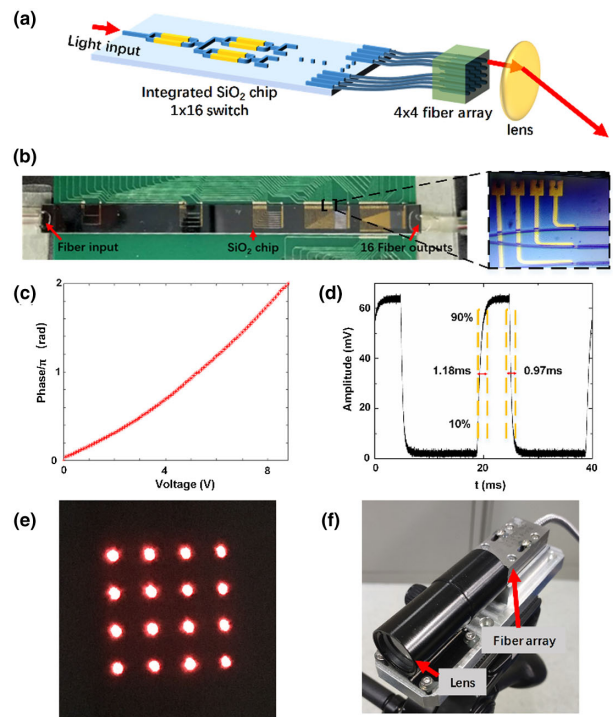


Fig. 2. (a) Setup of the LABS device. (b) Photo of the SiO_2 1×16 switch chip. Inset: microscopic image of part of the chip. (c) Measured phase shift versus different electrical voltage. (d) Measured switching waveform. (e) Output red spots for illustration purposes. (f) Packaged fiber array and lens.

array can also be replaced by an integrated chip with three-dimensional (3D) waveguides [22]. For illustration purposes, we inject 630 nm of red light into the beam-steering device; the output red spots after the fiber array can be clearly observed, as shown in Fig. 2(e). The fiber array has an equal spacing of 0.25 mm . Finally, a lens with a focal length of 40 mm and a diameter of 20 mm are added. Its focal plane is overlapped with the surface (i.e., emitter plane) of the fiber array. The corresponding beam steering step is 0.35° , and the total steering angle is $1.05^\circ \times 1.05^\circ$. The divergence angle of the beam after the lens collimation is 0.014° . The lens is packaged in a lens tube to isolate the off-axis scattering light, as shown in Fig. 2(f).

The whole photonic circuit assisted with a lens is an integrated transmitting and receiving a Lidar system. The light beams are emitted and received by the same aperture. As mentioned, the beam steering is achieved by controlling the switch and guiding the light to one of the 16 outputs. The 1×16 switch has a binary-tree structure consist of four stages of cascaded 1×2 MZI switches. The thermal phase shifters in the 1×2 MZI switches are driven by the self-developed electronic circuits. Briefly, the digital control signals for the switches are generated by a field-programmable gate array. These digital signals are then amplified and biased to meet the voltage requirement of the phase shifters. Each time only one 1×2 MZI switch in each stage is manipulated. Therefore, only four MZI switches are manipulated during the operation, i.e., $O(\log N)$ power consumption for N antennas. By switching the laser pulses to different channels on the 1×16 switch chip and then to different emitters on fiber array, different scanning angles are achieved.

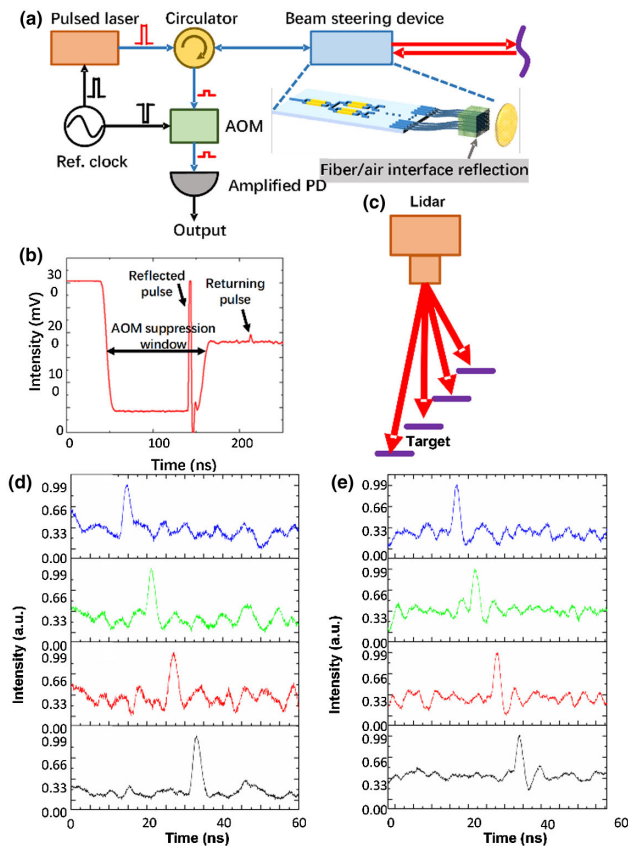


Fig. 3. (a) Setup of the Lidar system. (b) Typical output waveform of the photodetector. (c) Setup for the Lidar scanning test. (d) Four returning pulses at four different target distances and angles. (e) Four returning pulses scattered from a corner mirror at four different distances and angles.

The experimental setup of the LABS based Lidar is shown in Fig. 3(a). The whole Lidar system is based on coaxial ToF detection approach. A 1550 nm pulsed laser generates optical pulses with a peak power of 2 kW, a pulse width of 0.5 ns, and a repetition rate of 20 kHz. For the silica waveguide with a core size of $6\ \mu\text{m} \times 6\ \mu\text{m}$, this power level does not damage the waveguide. The pulsed laser is triggered by a reference clock for synchronization. The laser output is connected to a fiber circulator with an extinction ratio greater than 60 dB and then coupled into the switch chip through its input fiber. The high extinction ratio of the circulator is to suppress the crosstalk directly from the laser to the detector.

The pulsed light is then guided by the on-chip 1×16 switch and emit to free space by the 2D fiber array. At any time, the pulsed light is only routed to one fiber. The beam steering is achieved by switching the light to different output ports of the chip and emitting to the different position of the lens. The returning light after being scattered by a target (an A4 paper) is collected by the same lens inside the beam-steering device. Then the returning light is extracted by the fiber circulator, propagates through an acousto-optic modulator (AOM) and enters an amplified photodetector. It is noted that a 4% reflection appears in the interface of uncoated fiber array end facets and air. The peak power of the reflected pulses is high enough to saturate or even damage the amplified photodetector. Therefore, a shut-off electrical pulse from the same reference clock is synchronously

applied to the AOM to suppress the reflected light pulses. Figure 3(b) shows a typical output waveform of the photodetector when a target is placed at a distance of 10.5 m. The 100 ns wide suppression window generated by the AOM with the suppressed reflected pulse (generated by fiber/air interface) can be clearly seen. The amplitude of the reflected pulse can be further reduced by coating an antireflection coating on the facet of fiber array. This suppressed reflected pulse also plays a role of the reference signal in the time domain. The reflected pulse and the returning pulse scattered from the target are marked in the figure. The DC background is the amplified spontaneous emission (ASE) noise generated by the pulsed laser module. Limited by the constraint of experimental space, the measured maximum distance is 19.5 m. A maximum ranging distance of 200 m is potentially supported with the current system. In addition, if the avalanche photodetector is applied, the detection distance can be farther.

Furthermore, the beam-steering and ranging function of the Lidar are verified. As illustrated in Fig. 3(c), four matching targets (A4 paper) are placed in a distance range from 4.8 to 7.5 m with an interval of ~ 0.9 m. The beam-steering angles range from -0.53° to 0.53° . The measured returning pulses are shown in Fig. 3(d). The returning pulses have slightly different signal-to-noise ratios (SNRs) due to the uneven insertion loss of different channels caused by a fabrication error. A similar experiment is performed when a corner reflector is used as a target, as shown in Fig. 3(e). The power entering the photodetector is attenuated because the reflected power is very high and can saturate the photodetector.

In addition, we have further characterized the ranging resolution and lateral resolution of this Lidar. In ToF ranging, the timing error Δt has the following relationship with respect to the signal-to-noise ratio and signal rise time [23]:

$$\Delta t = \frac{\text{signal rise time}}{\text{signal} - \text{to} - \text{noise ratio}}. \quad (5)$$

Additionally, the corresponding ranging error is

$$\Delta R = \left(\frac{\Delta t}{2} \right) c. \quad (6)$$

For this experiment, the pulse width generated by the laser is 0.5 ns, and the signal rise time is ~ 0.25 ns. The worst SNR measured in the experiment is 1.9. The SNR is obtained by calculating the power ratio between the signal power (peak power of the returning pulse) and root-mean-square (rms) noise power with respect to the DC background. Therefore, according to Eqs. (5) and (6), the ranging error ΔR is about 2 cm. To verify the ranging accuracy, measurements are taken on a few stationary targets with the known space of 10 cm. The target distance ranging from 6.25 to 10 m. Figure 4(a) summarizes the relationship of the time delays between the reference signal and returning pulses at different target distances. The inset in Fig. 4(a) shows a zoomed view of 10 cm distance step. The linear relation can be clearly seen. The absolute error is no more than 3 cm within 10 m, which is limited by the low SNR of the scattered signal. The absolute error measurements show good agreement with the theoretical error.

The lateral distance resolution is dependent on the spot size on the lens plane and the beam divergence. By assuming an ideal

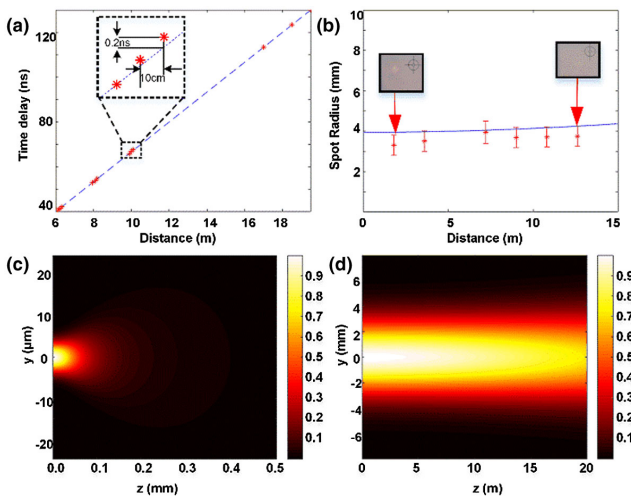


Fig. 4. (a) Time delays of returning pulses with respect to target distance. Inset: a zoomed view of a 10 cm distance step. (b) Measured (blue) and calculated (red) beam diameter at different distances. Inset: light spots on a near-infrared observation card at a distance of 1.8 and 12.6 m. (c) Calculated ideal Gaussian beam propagation (intensity) after the fiber. (d) Calculated ideal Gaussian beam propagation (intensity) after the lens.

Gaussian beam propagation when the light emits out of the fiber, the spot size d on the lens plane is given by [24]

$$d = 2\omega_0 \sqrt{1 + \left(\frac{f\lambda}{\pi\omega_0^2}\right)^2}, \quad (7)$$

where $\omega_0 = 5 \mu\text{m}$ is the radius of the waist of the Gaussian beam (single-mode fiber with $10 \mu\text{m}$ mode size), and $f = 40 \text{ mm}$ is the focal length. Thus, the spot size on the lens is $d = 7.9 \text{ mm}$ before being collimated by the lens. The theoretically calculated Gaussian beam propagation after the fiber is shown in Fig. 4(c), where the fiber end facet are located at $z = 0$. The far-field divergence angle of the Gaussian beam is calculated to be 0.2 rad (11.46°).

The beam after the collimation of the lens is also calculated by using thin lens transformation and ABCD law, as shown in Fig. 4(d), where the lens is located at $z = 0$. The beam divergence is 0.25 mrad (0.014°) based on Eq. (2). The beam diameter expansion due to the beam divergence after 20 m is $0.25 \text{ mrad} \times 20 \text{ m} = 5 \text{ mm}$. Experimentally, the light spots are observed by a laser viewing card (Thorlabs VRC4). The spot size is measured by measuring the beam size on the viewing card, as shown in Fig. 4(b). The theoretical beam radius calculated by Gaussian beam propagation is also plotted. It can be seen that the beam radius is almost unchanged at $\sim 4 \text{ mm}$ within the range of 13 m . It should be noted that due to the power decay of the luminescence light on the viewing card, the measured beam radius is estimated to have a uncertainty of $\sim 0.5 \text{ mm}$.

In conclusion, a solid-state Lidar system based on 2D LABS is demonstrated at 1550 nm . The beam-steering device consists of a SiO_2 switch chip, a fiber array for 1D to 2D conversion, and a lens. The Lidar is operating under ToF mode. The Lidar has a maximum measurement distance of 19.5 m limited by the experimental space, 4×4 scanning points and a maximum

scanning angle of 1.05° . The scanning points and angle can be scaled to large numbers by increasing the number of output ports and changing the lens parameters. The fiber array can also be replaced by an integrated 3D waveguide array. This Letter indicates the feasibility of Lidar application based on LABS technology and may pave the way for a practical high-performance solid-state Lidar system.

Funding. National Natural Science Foundation of China (61535006, 61875122, 61922056).

Disclosures. The authors declare no conflicts of interest.

REFERENCES

- M. A. Lefsky, W. B. Cohen, G. G. Parker, and D. J. Harding, *Bioscience* **52**, 19 (2002).
- J.-F. Lalonde, N. Vandapel, D. F. Huber, and M. Hebert, *J. Field Robot.* **23**, 839 (2006).
- X. Chen, H. Ma, J. Wan, B. Li, and T. Xia, *Conference on Computer Vision and Pattern Recognition (IEEE, 2017)*, pp. 1907–1915.
- M. Jofre, G. Anzolin, F. Steinlechner, N. Oliverio, J. P. Torres, V. Pruneri, and M. W. Mitchell, *Opt. Express* **20**, 12247 (2012).
- C. Errando-Herranz, N. Le Thomas, and K. B. Gylfason, *Opt. Lett.* **44**, 855 (2019).
- Y. Wang, G. Zhou, X. Zhang, K. Kwon, P.-A. Blanche, N. Triesault, K.-S. Yu, and M. C. Wu, *Optica* **6**, 557 (2019).
- J. A. Frantz, J. D. Myers, R. Y. Bekele, C. M. Spillmann, J. Naciri, J. Kolacz, H. G. Gotjen, V. Q. Nguyen, C. C. McClain, L. Brandon Shaw, and J. S. Sanghera, *J. Opt. Soc. Am. B* **35**, C29 (2018).
- J. Sun, E. Timurdogan, A. Yaacobi, E. S. Hosseini, and M. R. Watts, *Nature* **493**, 195 (2013).
- D. N. Hutchison, J. Sun, J. K. Doyle, R. Kumar, J. Heck, W. Kim, C. T. Phare, A. Feshali, and H. Rong, *Optica* **3**, 887 (2016).
- A. Yaacobi, J. Sun, M. Moresco, G. Leake, D. Coolbaugh, and M. R. Watts, *Opt. Lett.* **39**, 4575 (2014).
- J. Xu, M. Cua, E. H. Zhou, Y. Horie, A. Faraon, and C. Yang, *Opt. Lett.* **43**, 5255 (2018).
- W. Xu, L. Zhou, L. Lu, and J. Chen, *Opt. Express* **27**, 3354 (2019).
- T. Komljenovic, R. Helkey, L. Coldren, and J. E. Bowers, *Opt. Express* **25**, 2511 (2017).
- D. Inoue, T. Ichikawa, A. Kawasaki, and T. Yamashita, *Opt. Express* **27**, 2499 (2019).
- C. Li, X. Cao, K. Wu, X. Li, and J. Chen, *Opt. Express* **27**, 32970 (2019).
- H. Ito, Y. Kusunoki, J. Maeda, D. Akiyama, N. Kodama, H. Abe, R. Tetsuya, and T. Baba, *Optica* **7**, 47 (2020).
- E. H. Cook, S. J. Spector, M. G. Moebius, F. A. Baruffi, M. G. Bancu, L. D. Benney, S. J. Byrnes, J. P. Chesin, S. J. Geiger, D. A. Goldman, A. E. Hare, B. F. Lane, W. D. Sawyer, and C. R. Bessette, *J. Microelectromech. Syst.* **29**, 1008 (2020).
- J. J. López, S. A. Skirlo, D. Kharas, J. Sloan, and C. Sorace-Agaskar, *Conference on Lasers and Electro-Optics (CLEO): Science and Innovations (2018)*.
- Y.-C. Chang, M. C. Shin, C. T. Phare, S. A. Miller, and M. Lipson, *Conference on Lasers and Electro-Optics (CLEO): Science and Innovations (2019)*.
- S. Kim, J. Sloan, J. J. López, D. Kharas, and M. Soljačić, *Conference on Lasers and Electro-Optics (CLEO): Science & Innovations (2019)*.
- C. V. Poulton, A. Yaacobi, D. B. Cole, M. J. Byrd, M. Raval, D. Vermeulen, and M. R. Watts, *Opt. Lett.* **42**, 4091 (2017).
- M. Pospiech, M. Emons, B. Väckenstedt, G. Palmer, and U. Morgner, *Opt. Express* **18**, 6994 (2010).
- H. N. Burns, *Opt. Eng.* **30**, 323 (1991).
- E. Hecht, *Optics* (Addison Wesley, 2002), Chap 13.